aerospace

MDPI

Article

A Comprehensive Study on the Aerodynamic Characteristics of Electrically Controlled Rotor Using Lattice Boltzmann Method

Lingzhi Wang and Taoyong Su *

School of General Aviation, Nanchang HangKong University, Nanchang 330063, China; linzhi656@163.com
* Correspondence: sutaoyong@nchu.edu.cn; Tel.: +86-0791-83863210

Abstract: An electrically controlled rotor (ECR) is a kind of swashplateless rotor that implements the primary control via the trailing-edge flap system instead of a swashplate and demonstrates great potential in vibration reduction and noise alleviation. In this paper, the mesoscopic numerical simulation method known as the lattice Boltzmann method (LBM) is employed to investigate the aerodynamic characteristics of an ECR. In the LBM, the discretized Boltzmann transport equation is solved to simulate the macroscopic motion of the fluid, and the D3Q27 model is applied for this study. The effects of the flap deflection on the ECR aerodynamic characteristics can be accurately included with the appropriate refined wall lattice resolution. On this basis, the adaptive wake-refinement strategy is applied to track the evolution of the wake and adequately capture details of the wake structure in the wake flow field. Based on this method, an aerodynamic analysis model for the ECR can be established on the XFlow simulation platform. The aerodynamic analysis model is validated, and the results indicate that the LBM can accurately capture the details of the rotor flow field and calculate blade aerodynamic load, as well as predict the downwash of the rotor. Therefore, based on this model, the ECR aerodynamic characteristics under hovering and forward flight conditions are analyzed, and the effects of the flap deflection on the wake structure, induced inflow, and disc load can be captured. The results indicate that a relatively large flap deflection required to trim the rotor will cause the additional intense flap wake vortex in the ECR wake flow field, apart from the concentrated vorticity at the blade tip and root demonstrated in the conventional rotor wake flow field, and thus significantly change the distributions of the disc-induced inflow and aerodynamic load.

Keywords: electrically controlled rotor (ECR); lattice Boltzmann method; adaptive wake-refinement strategy; trailing-edge flap

check for updates

Citation: Wang, L.; Su, T. A Comprehensive Study on the Aerodynamic Characteristics of Electrically Controlled Rotor Using Lattice Boltzmann Method. *Aerospace* **2023**, *10*, 996. https://doi.org/10.3390/aerospace10120996

Academic Editors: Chen Wang, Michael I. Friswell and Jiaying Zhang

Received: 13 October 2023
Revised: 24 November 2023
Accepted: 25 November 2023
Published: 28 November 2023

1. Introduction

The electrically controlled rotor (ECR), also known as the swashplateless rotor, is a promising new concept of rotor controlling system proposed at the beginning of this century [1]. Unlike conventional rotor control systems, ECR implements primary flight control via an integrated trailing-edge flap instead of a swashplate. In the ECR trailing-edge flap system, the electrical actuator mounted near the blade root generally drives the flap to generate an aerodynamic pitching moment to indirectly change the blade pitch. As the swashplate is removed, the rotor controlling system can be greatly simplified, which effectively decreases the parasite drag of the helicopter and maintenance requirements [2]. Additionally, research shows that the trailing-edge flap has significant potential to be used for active vibration reduction [3,4], noise alleviation [5,6], and performance enhancement [7,8].

However, due to the introduction of the trailing-edge flap, the aerodynamic characteristics of ECR are more complex compared to the conventional rotors. During the process of primary flight control, the trailing-edge flap operates in a severely unsteady aerodynamic environment, especially in the forward fight condition at high speed, and flap deflection will cause great changes in the wake flow field of ECR. Within the wake flow field, interference occurs not only between the rotor blade and wake but also between the flap and wake, which further influences the distributions of the disc load and induced inflow. Therefore, it is necessary to accurately take the effects of flap deflection on the distribution of the disc load and the induced inflow into account, which will contribute to research on ECR vibration reduction, noise alleviation, and performance improvement.

In recent years, researchers have extensively carried out numerous investigations associated with the aerodynamic characteristics of ECR. In 2001, Ormiston first conducted a theoretical investigation on the feasibility of the ECR concept based on a simple two-dimensional quasi-steady airfoil theory and uniform inflow model [1]. Shen and Chopra conducted further comprehensive research on the ECR aerodynamics and key design parameters utilizing the UMARC. The research indicated that the appropriate trailing-edge flap input can not only successfully achieve rotor trim but also can significantly achieve vibration reduction while also verifying the feasibility of the trailing-edge flap to simultaneously implement ECR primary flight control and active vibration control [9–11]. Subsequently, building upon Shen's research, Falls and Chopra further developed the ECR aerodynamics analysis model [12]. They initially employed the computational fluid dynamics (CFD) method to establish a numerical wind tunnel data table for an airfoil with a flap. Then, to accurately account for the impact of flap deflection on the wake flow field and vortex circulation distribution at blade boundaries, two vortices shed by both sides of the flap were introduced based on the free wake model proposed by Bagai [13]. Moreover, based on the aforementioned aerodynamics models, the ECR performance was investigated [14]. Recently, to take the wake viscous effect into account and not rely on empirical parameters anymore, another ECR aerodynamics model based on the viscous vortex particle method (VVPM) and Weissinger-L blade lifting surface model was proposed by Su [15].

As mentioned above, the CFD and free wake methods have been widely used to analyze the aerodynamic characteristics of the ECR. The CFD method has the significant potential to accurately capture the unsteady characteristics of rotor wake structure and calculate corresponding induced inflow. Therefore, it has been widely employed in conducting comprehensive rotorcraft aerodynamics analysis. However, to accurately simulate the flap deflection and take the effects of flap deflection on the ECR aerodynamics characteristics into account, various mesh techniques, including overset mesh, sliding mesh, and dynamic mesh, are required to be employed, and the mesh between the blade and flap needs to be refined, which will increase computational instability and time. Additionally, due to the inherent numerical dissipation, the rotor wake will dissipate prematurely, which cannot afford sufficient details of the rotor far wake to analyze. The free wake method possesses the characteristics of effectively calculating the complex rotor wake structures and capturing the unsteady rotor wake with high precision. Nevertheless, it is based on the assumption of potential flow and cannot include the viscous effect; its results rely on the empirical parameters. Although the VVPM can effectively address the problems of the free wake method in the rotor aerodynamic analysis, it still employs empirical parameters in terms of calculating aerodynamic load with inherent errors in the results.

Over the past two decades, LBM has demonstrated its great potential in simulating complex fluid flows and modeling the Navier–Stokes equations, gradually emerging as a promising numerical simulation method. Moreover, it has been widely employed in various fields, including multiphase flows [16], turbulence [17], microscale fluids [18], and beyond. Unlike those conventional CFD methods based on the continuous medium hypothesis, the LBM is a numerical simulation method built on the mesoscopic level, which provides a new perspective to better understand and capture more details of physical fluid flow phenomena. Therefore, researchers have employed this method to analyze the rotorcraft aerodynamics characteristics in recent years, mainly focusing on the blade vortex interaction [19], helicopter noise [20], and wake structure [21]. However, there is no relevant literature on the characteristics of ECR aerodynamics based on the LBM; thus, to overcome the shortcomings of the aforementioned methods in predicting the ECR wake flow field and calculating the corresponding induced inflow, an analysis model for the aerodynamic characteristics of ECR based on LBM is established. In this paper, the effects of flap deflection can be included by adaptively refining the lattice resolution near the flap; the detailed lattice resolution will be described in Section 2. Additionally, more details of the ECR wake flow field can be captured effectively and accurately due to lower numerical dissipation and parallel computation of the LBM compared to the aforementioned methods. The research in this paper focuses on the effects of different blade pre-index angles in the hovering state and various advance ratios on the aerodynamic characteristics and wake structure of the ECR.

This paper is organized as follows. First, the numerical method and the establishment of the ECR aerodynamic analysis model based on the LBM will be described in Section 2. Next, as there are no relevant experiment data on the ECR test, to validate the capability of the LBM for predicting rotor flow field and calculating corresponding induced inflow and blade aerodynamic load, the validations of the Caradonna–Tung rotor and 2MRTS rotor will be described in Section 3. On this basis, the effects of various blade pre-index angles and advance ratios on the wake structure, disc load, and induced inflow distribution of the ECR will be investigated in this paper. Finally, conclusions based on the aforementioned research are drawn.

2. ECR Aerodynamic Analysis Model Based on the Lattice Boltzmann Method

2.1. Lattice Boltzmann Method

The LBM is a mesoscopic numerical simulation method. Unlike the traditional CFD methods, which numerically solve the governing equations to simulate the fluid dynamic behavior, the LBM based on the Boltzmann transport equation models the fluid consisting of a large number of microscopic particles with random motions, and such particles perform consecutive streaming and collision processes over a discrete lattice grid, thus describing the macroscopic properties of the fluid. Moreover, the motion behavior of the collection of particles is determined by the probability distribution functions (PDFs), $f_i(\vec{x}, \vec{e}, t)$, where $\vec{x}$ represents the space position vector, e_i is the discrete velocity at position x, and t is the time.

In the LBM, the discretization of space, time, and velocity needs to be employed to solve the Boltzmann transport equation. Therefore, the Boltzmann transport equation can be discretized into a lattice Boltzmann equation, which can be written as

$$f_i(\vec{x} + \vec{e}_i\delta t, t + \delta t) - f_i(\vec{x}, t) = \delta t \Omega_i(x, t) \tag{1}$$

where Ω_i represents the collision operator, and e_i is the discrete velocity along the ith direction. Equation (1) is difficult to solve for its complicated collision term; to simplify the equation, the simplified model for the collision operator with the Bhatnagar–Gross–Krook (BGK) approximation is introduced [22]. The basic assumption is that the outcome of the particles' collisions tends towards the Maxwell–Boltzmann equilibrium distribution. The BGK collision operator is widely employed for most LBM but exhibits several limitations for high Reynolds number flows. For this study, the multiple-relaxation time with central moments (MRT-CM) is introduced to overcome some limitations of the BGK method. The MRT-CM is implemented in central-moment space, which can provide a low numerical dissipation and enhance stability [23]. Moreover, the simulation of higher Reynolds and Mach number flows can be achieved through the MRT-CM implementation compared with the BGK approach. The MRT-CM collision operator can be described as follows:

$$\Omega_{f_j}^{\text{MRT-CM}} = M_{jk}(\mathbf{u})^{-1} S_{kl} M_{li}(\mathbf{u})(f_i^{eq} - f_i) \tag{2}$$

With the MRT-CM approximation, Equation (1) can be written as

$$f_i(\vec{x} + \vec{e}_i\delta t, t + \delta t) - f_i(\vec{x}, t) = \delta t \Omega_{f_j}^{\text{MRT}-\text{CM}} \tag{3}$$

where f_i^{eq} is the local equilibrium distribution function, M_{ij} represents the transformation moment matrix, and S_{ij} is the diagonal relaxation matrix; the detailed implementation of the MRT-CM can be found in Ref. [24]. Equation (3) can normally be divided into two steps in the implementation of the LBM [25]: The first step is streaming (the left side in Equation (3)), which means that the particles move from one lattice to another adjacent lattice node within the specific discrete velocity in a single timestep. Subsequently, they collide with other particles arriving at the same lattice node from different directions according to the collision rules, exchanging the energy and momentum and generating a new PDF in the process of the collision. The detailed process is demonstrated in Figure 1.

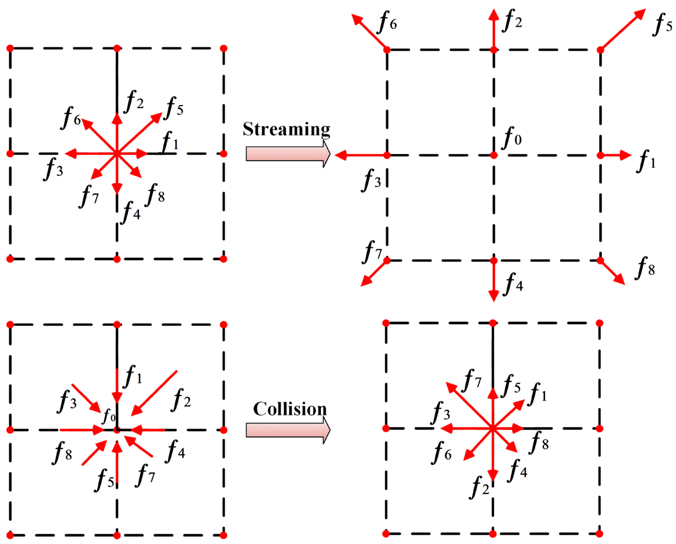

Figure 1. The process of streaming and collision (D2Q9 model).

The basic model of the LBM introduced by Qian [26] is described as DnQm, where n represents the dimension, and m stands for the number of discrete velocities. This paper implements the numerical simulation of the ECR wake flow field in the XFlow simulation platform based on the LBM. Its lattice model, D3Q27, illustrated in Figure 2, is equipped with characteristics of highly symmetric and more discrete velocities compared to other lattice models, which can improve the stability and accuracy of the numerical simulation but might increase the computational cost and time. Overall, these features make it suitable for the ECR aerodynamics analysis.

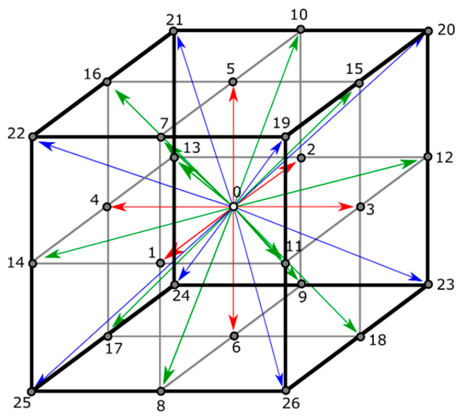

Figure 2. D3Q27 LBM model (The numbers 0 to 26 represent the discrete velocity vectors in 27 directions).

The discrete velocity vectors e_i and corresponding weight factors w_i, according to Ref. [27], are defined as follows:

$$e_i = \begin{cases} (0,0,0) & i = 0 \\ (\pm1,0,0)c,\ (0,\pm1,0)c,\ (0,0,\pm1)c, & i = 1,2,3\ldots6 \\ (\pm1,\pm1,0)c,\ (0,\pm1,\pm1)c,\ (\pm1,0,\pm1)c, & i = 7,8,9\ldots18 \\ (\pm1,\pm1,\pm1)c, & i = 19,20,21\ldots26 \end{cases} \tag{4}$$

$$w_i = \begin{cases} 8/27, & i = 0 \\ 2/27, & i = 1,2,3\ldots6 \\ 1/54, & i = 7,8,9\ldots18 \\ 1/216, & i = 19,20,21\ldots26 \end{cases} \tag{5}$$

where c represents the lattice sound speed, which is normally assumed to be 1. The discrete velocity vectors, PDFs, and weight factors of the D3Q27 lattice model can be employed to further calculate the macroscopic fluid density, velocity, and local equilibrium distribution function as illustrated in Equations (6) and (7) [28].

$$\rho(\vec{x},t) = \sum_{i=0}^{k} f_i(\vec{x},t),\ \vec{u}(\vec{x},t) = \frac{1}{\rho}\sum_{i=0}^{k} c f_i \vec{e}_i \tag{6}$$

$$f_i^{eq}(\vec{x},t) = \rho w_i\left[1 + 3(e\cdot u) + \frac{9}{2}(e\cdot u)^2 - \frac{3}{2}u^2\right] \tag{7}$$

The common procedure to simulate the ECR flow field utilizing the LBM can be described as follows. First, the macroscopic density, velocity, and local equilibrium distribution functions of the computational fluid domain are initialized. Next, new PDFs can be obtained during the process of the streaming step. Subsequently, new macroscopic density, velocity, and local equilibrium distribution functions can be calculated by employing the aforementioned new PDFs and Equations (6) and (7). Finally, the process of the particle collision is applied to generate the new PDFs; then, repeat the above steps until convergence and export the calculation results.

2.2. Turbulence Modeling

To capture the unsteady flow phenomenon of the ECR flow field, the approach called the large eddy simulation (LES) is employed in this paper. This method introduces an additional turbulence eddy viscosity to model the sub-grid turbulence. Moreover, the consistent local eddy viscosity and near-wall behavior can be investigated by applying the turbulence model called the wall-adapting local eddy viscosity model (WALE) [29]. The detailed implementation can be described as follows:

$$\nu_t = (C_w \Delta x)^2 \frac{(G^d_{\alpha\beta}G^d_{\alpha\beta})^{3/2}}{(S_{\alpha\beta}S_{\alpha\beta})^{5/2} + (G^d_{\alpha\beta}G^d_{\alpha\beta})^{5/4}} \tag{8}$$

$$G^d_{\alpha\beta} = \frac{1}{2}(g^2_{\alpha\beta} + g^2_{\beta\alpha}) - \frac{1}{3}\delta_{\alpha\beta}g^2_{\gamma\gamma} \tag{9}$$

$$S_{\alpha\beta} = \frac{g_{\alpha\beta} + g_{\beta\alpha}}{2} \tag{10}$$

$$g_{\alpha\beta} = \frac{\partial u_a}{\partial x_\beta} \tag{11}$$

where C_w is the constant, normally assumed to be 0.325, and Δ stands for the cell-size scale. $G_{\alpha\beta}$ and $S_{\alpha\beta}$ represent the strain rate tensors associated with the resolved scales, and $\delta_{\alpha\beta}$ is the Kronecker symbol.

2.3. Establishment of the ECR Aerodynamic Analysis Model

The modified full-scale Z–11 helicopter rotor is selected as a reference to model the ECR for the numerical simulation. As the time cost and computational complexity of aeroelastic coupling and simulation are significant, the blade deformation is neglected to simplify the problem. For this study, the rigid blade model is employed. The ECR model consists of three blades with an NACA0012 airfoil section of a chord length *c* of 0.35 m and a linear twist of $-12°$ from the root cutout to the blade tip. The rotor radius is 5.345 m, and the rotational speed is 400 rpm, corresponding to a blade tip Mach number of 0.659. Moreover, the NACA0012 airfoil is also selected for modeling the flap; the flap span, chord, and midspan locations are 0.0875 m, 1.069 m, and 3.7415 m, respectively. The detailed parameters for the ECR model are shown in Figure 3.

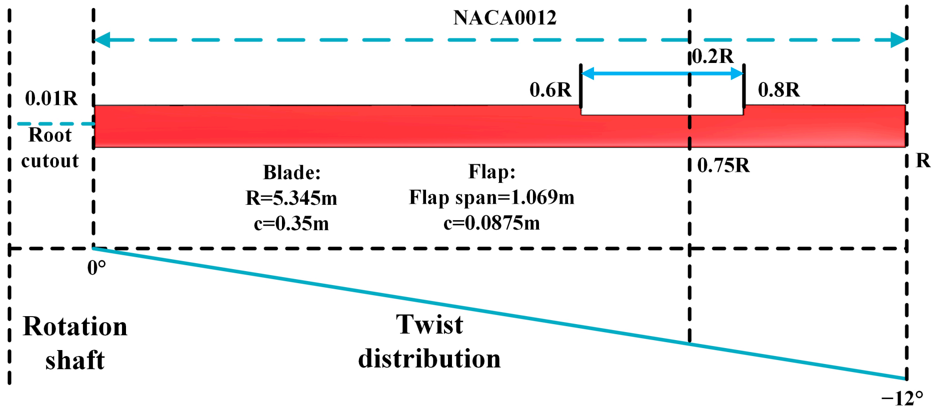

Figure 3. The parameters of the ECR model.

The virtual wind tunnel illustrated in Figure 4 is employed for the numerical simulation with the size of $80 \times 40 \times 40$ m in the Z, Y, and X directions, respectively, to avoid the wall effect. The free stream direction is from $-Z$ to $+Z$, and the different advance ratios in forward flight conditions can be simulated by setting different wind speeds. For the hovering conditions, the wind speed is set to 0. As for the setup of the flow field and boundary conditions, the flow environment in this paper is set as the single-phase, isothermal, and external flow, and the inlet and outlet boundary conditions are set as the velocity inlet and zero-gauge-pressure outlet, respectively. The periodic boundary condition is applied for the other four planes. In addition, the non-equilibrium enhanced wall function for the blade and flap wall boundary condition is employed to include the effect of the pressure gradients in the flow separation prediction. In terms of other simulation settings, the time step is set to 0.00125 s, which means that calculation results can be acquired with an azimuthal step of 3°. The total simulation time is 1.2 s, which corresponds to the time of eight revolutions. Moreover, the inputs of the blade and flap, including collective pitch, lateral cyclic pitch, and longitudinal cyclic pitch, for the hover and forward flight conditions will be thoroughly described in Section 3.

The spatial lattice resolution requires the appropriate arrangement to guarantee the accuracy of the numerical simulation results and effectively capture more details of the flow field. Generally, to enhance the computational precision, the lattice resolution needs to be as refined as possible during the process of simulation. However, the higher level of refinement will significantly increase the number of elements, which demands a substantial amount of computational time and resources. Therefore, under the premise of ensuring computational accuracy and efficiency, a relatively coarse lattice resolution of 1.28 m is applied to the far field, and the lattice resolution refined strategy is only employed for the blade surface (resolution of 0.01 m), flap surface (resolution of 0.01 m), and wake flow field (resolution of 0.01 or 0.02 m). In particular, the adaptive wake-refinement strategy, which can dynamically refine the wake, is applied to investigate the evolution of the wake generated by the blade or flap. The detailed lattice resolutions are shown in Figure 5.

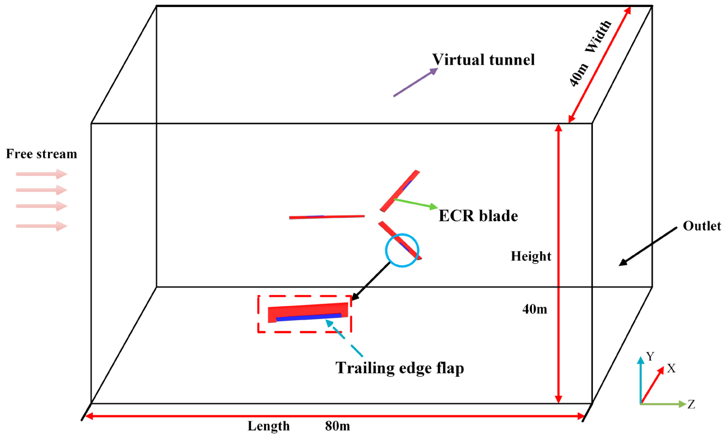

Figure 4. Computational domain for the ECR model.

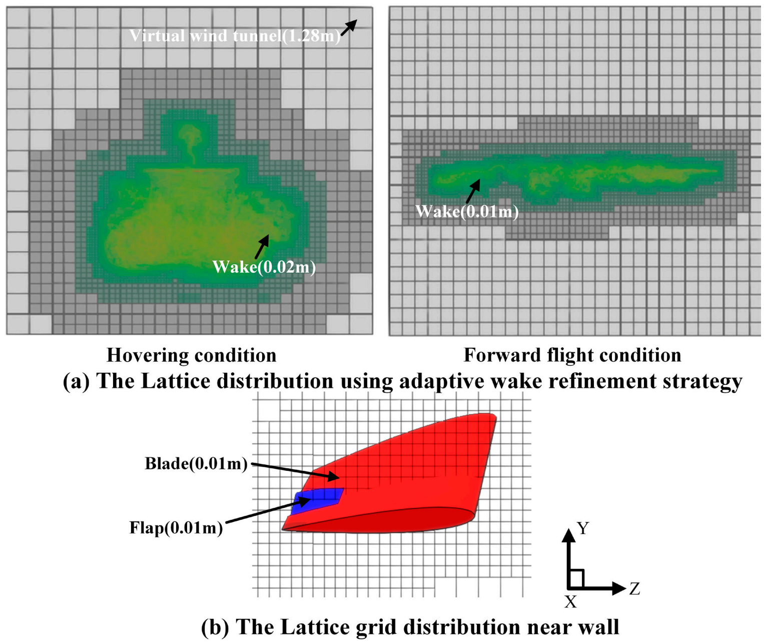

Figure 5. Lattice resolution arrangement for the numerical simulation.

3. Numerical Results and Analysis

3.1. Validation of Caradonna–Tung Rotor in Hover

In this section, to validate the capability of LBM for calculating aerodynamic load and capturing the details of the wake structure, the well-known Caradonna–Tung rotor experiment in hover is selected as an example [30]. The blade pressure distribution and complex wake structure are calculated employing the aforementioned aerodynamic analysis model based on the LBM. The detailed simulation parameters for the Caradonna–Tung rotor are listed in Table 1.

Table 1. The main simulation parameters of the Caradonna–Tung rotor.

Parameters	Values
Rotor radius	1.143 m
Blade chord	0.1905 m
Blade airfoil section	NACA0012
Blade twist	0°
Blade collective pitch	8°
Root cutout	0.188 m
Rotor rotational speed	1250 rpm
Number of blades	2

Figure 6 illustrates the pressure coefficient Cp distributions at two blade spanwise locations (r/R = 0.96, r/R = 0.89) with the experimental data for comparison; it can be observed that the pressure distributions on the pressure side exhibit a good agreement with the experimental data and are relatively insensitive to the quality of the mesh, except for the peak prediction on the leading edge. However, a large difference and the fluctuation can be seen on the suction side, especially at the leading edge; the major reason for the discrepancy is that the suction side exhibits a severe flow detachment, and the relatively coarse grid cannot accurately capture the flow behavior at the leading edge. Figure 7 presents the friction coefficient Cf distributions to further investigate the underestimation of the Cp distributions. Within the Δx or Δx_1 region, the Cf initially decreases dramatically, corresponding to a relatively large adverse pressure gradient, which reduces the airflow velocity towards the trailing edge, causing the Cp to increase. Subsequently, it increases slowly and declines again, forming a small hump, which implies the phenomenon of flow separation and reattachment, resulting in the decrease and subsequent increase in the Cp. The peak of the hump will decline due to the reduced external velocity, and thus the amplitude of the Cp increase will diminish. Additionally, the peak Cp can be predicted accurately with the improvement in mesh quality. It means that the spatial lattice resolution employed for this study can accurately predict the aerodynamic load within an acceptable range of error but may not accurately predict the flow behavior at the leading edge. The fluctuation may decrease, and the pressure distributions may be better in agreement with the experimental data with the further refinement of lattice resolution. Nevertheless, the extra fine lattice resolution is not employed, taking into account the computational resources and numerical simulation time, which will be the future work to be conducted.

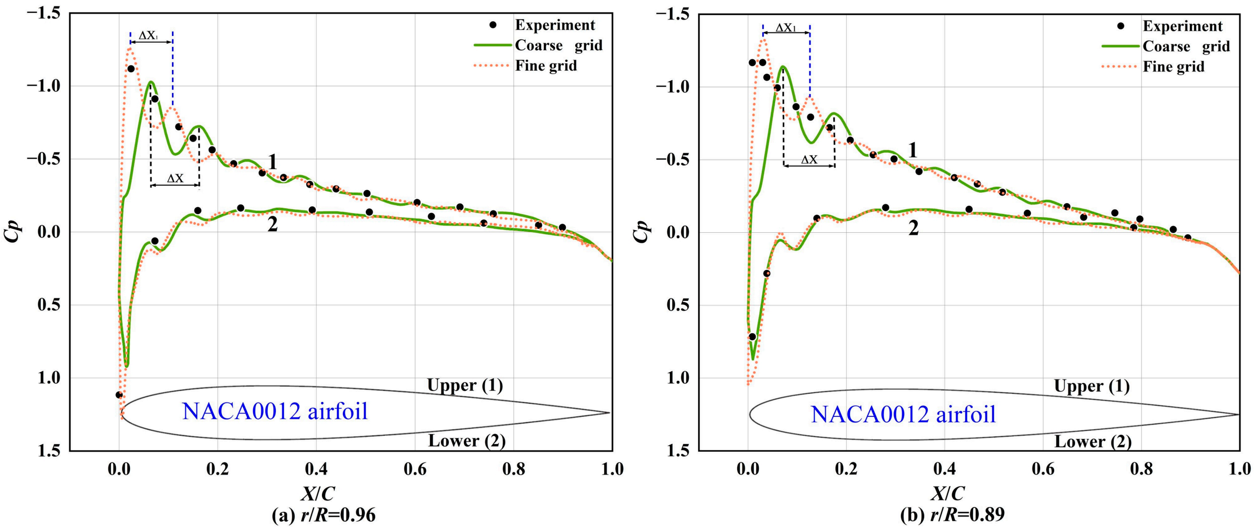

Figure 6. Pressure coefficient distributions at different blade spanwise locations.

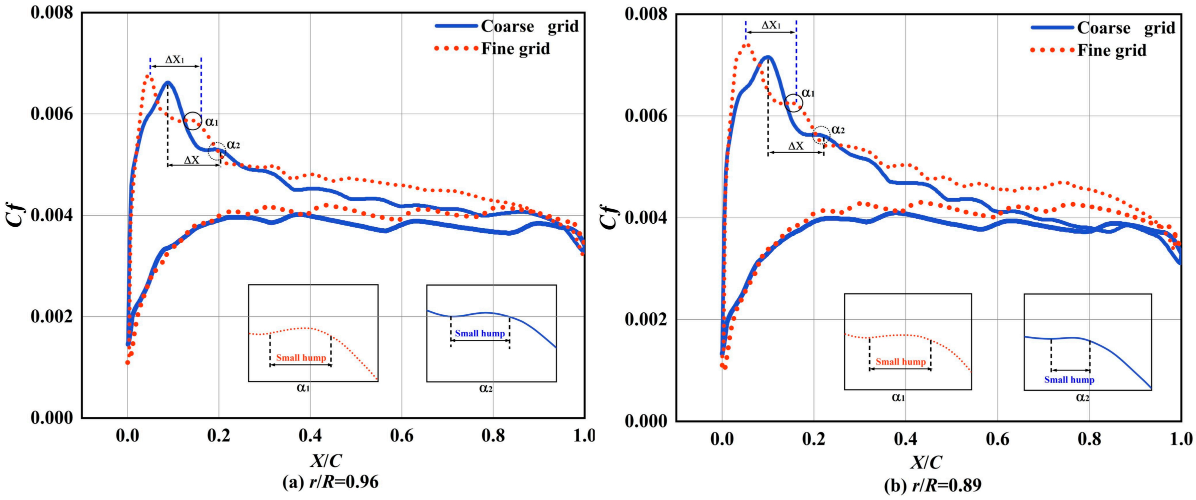

Figure 7. Friction coefficient distributions at different blade spanwise locations.

The wake structure of the Caradonna–Tung rotor is predicted by the LBM, with the CFD results for comparison presented in Figure 8. As shown in Figure 8a, the rotor wake exhibits a helicoidal structure and can be preserved for a long time. The characteristics of both the near and far wake can be observed compared to the CFD method. In Figure 8b, the tip vortices shed by the blades initially demonstrate symmetry and quickly contract. As the rotor wake migrates downstream, the tip wake becomes mutually entangled to form unstable vortex pairs due to the close distance between the tip vortices, causing the breakdown of the far wake structure. Ultimately, the rotor wake dissipates in the far field. The aforementioned results demonstrate that the LBM is capable of adequately capturing more details of the rotor wake and tracking the evolution of the rotor wake within the flow field.

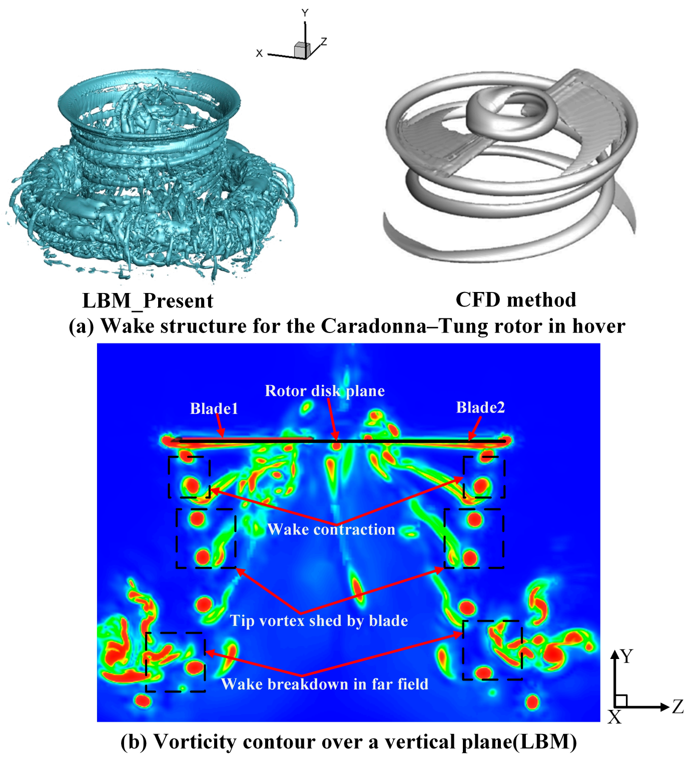

Figure 8. Wake structure predicted by the LBM and CFD method.

Finally, the calculation time for the LBM and conventional CFD method [31] for the 8° collective pitch and 1250 rpm case is documented in Table 2. As can be observed in Table 2, with the refinement of lattice spatial resolution, the computational time of the LBM significantly increases while the computational accuracy substantially improves. It is noted that the adaptive wake-refinement strategy is employed to adequately capture the details of the unsteady rotor wake, which will significantly increase the number of elements in the fine grid. It can be the main reason for the significant increase in the numerical simulation time. However, compared to the CFD method, the calculation efficiency improves with better precision.

Table 2. Calculation efficiency for the LBM and CFD method.

Method	Relative Error of CT, θ_0 = 8°	CPU Time/h	Computation Platform
LBM-Coarse grid	4.3%	15	64 Cores
LBM-Fine grid	1.2%	36	64 Cores
CFD-Fine grid	2.3%	64	64 Cores

3.2. Validation of 2MRTS Rotor in Forward Flight

As there are no relevant experimental data on the ECR-induced inflow distributions, to further validate the LBM in terms of calculating induced velocity, the 2MRTS rotor experiment in forward flight conditions is selected as a reference; the main rotor is composed of four blades featuring NACA0012 airfoil, with a chord length of 0.066 m [32]. The rotor radius, linear twist, and rotational speed are 0.86 m, −8°, and 2112 rpm, respectively. The simulation mainly focuses on the situation of an advance ratio of 0.15.

Figure 9 presents the induced inflow distributions normal to the tip path plane (TPP) at different azimuths, with the experimental data and CFD results [33] for comparison. The measuring plane is located at 1.15 chord lengths above the TPP, and the induced velocities normalized by the blade Mach number can be obtained through test points distributed at various blade spanwise locations. The results show that the induced inflow distributions at different azimuths calculated via the LBM relatively match the experimental data well in terms of the magnitude and trend. However, the underprediction of the induced inflow can be observed at the azimuthal angle of 0°. The location of test points at the azimuthal angle of 0° is directly downstream of the rotor disc. Viscous effects such as wake generated in the region of the rotor rotation center are believed to be responsible for some of the discrepancy. The same phenomenon can be observed in Ref. [34]. Moreover, minor deviations can also be observed compared to CFD calculation results. The main reason is that the effect of the fuselage is not included in the simulation. The calculation results of the induced inflow demonstrate that the LBM can predict the downwash of the rotor with high precision and further validate the aerodynamic analysis model established in this paper.

3.3. Analysis of ECR Aerodynamic Characteristics in Hover

As described in previous sections, the LBM demonstrates its capability in calculating the induced inflow and predicting the rotor wake structure and unsteady aerodynamic loads. Therefore, the effects of various blade pre-index angles in the hovering state on the wake structure, induced inflow, and aerodynamic loads of ECR will be investigated in this section. The wind tunnel trim strategy is employed to trim the ECR under hover conditions, and the trim target variables C_T, β_{1s}, and β_{1c} are 0.004126, 0, and 0, respectively. For the current research, the schemes of the blade pre-index angles of 4° and 12° are selected to investigate the aerodynamic characteristics of the ECR in hover conditions. The trim results of the ECR in hover conditions, with the conventional rotor for comparison, are shown in Table 3.

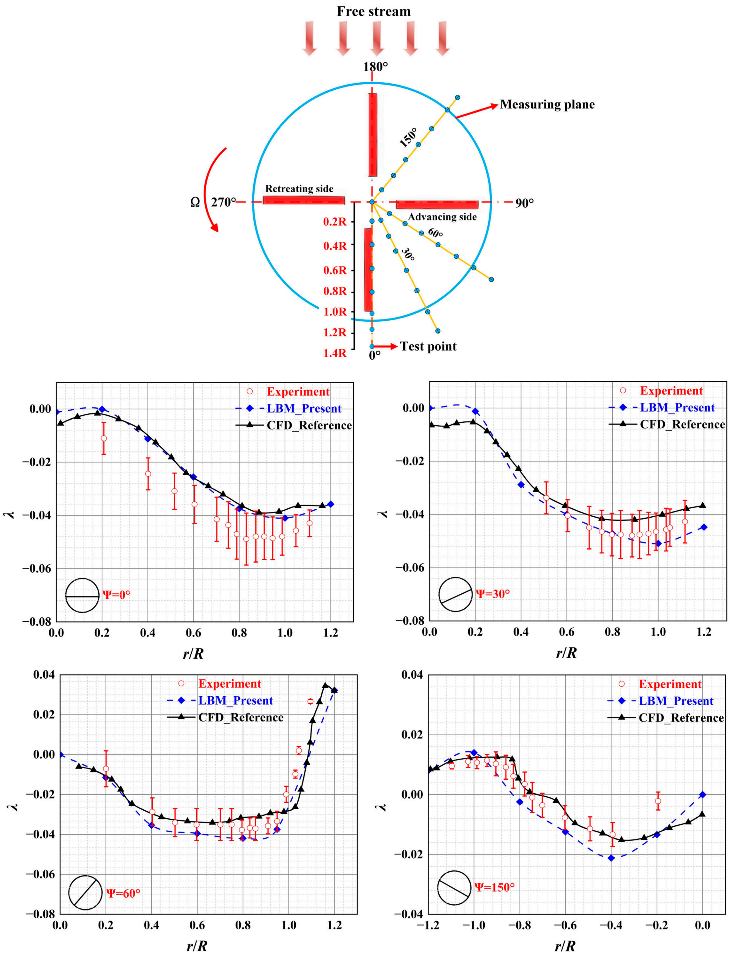

Figure 9. Induced inflow distributions at different azimuths above the TPP.

Table 3. The trim results of the ECR and conventional rotor in hover conditions.

	Blade Pre-Index Angle/°	Flap Collective Pitch/°	Blade Collective Pitch/°
ECR	4	−10.46	9.46
ECR	12	4.96	7.41
Conventional rotor			7.92

As illustrated in Table 3, the ECR differs from the conventional rotor in its mode of blade pitch control, which is indirectly implemented through the change in the flap deflection. Furthermore, the flap collective pitch trim variables exhibit a significant variation under different blade pre-index angles. When the blade pre-index angle is small, a significant negative deflection of the flap is required to achieve the desired blade collective pitch for trim, which indicates that the upward deflection of the flap generates a nose-up moment to increase the blade collective pitch. Conversely, when the blade pre-index angle is large, the downward deflection of the flap generates a nose-down moment and thus decreases the blade collective pitch to achieve the trim condition. In addition, the minor differences in the blade collective pitch at various blade pre-index angles can be observed due to the diverse additional aerodynamic forces generated by the different flap deflections.

The wake flow field and disc-induced inflow distributions will significantly differ due to the difference in flap collective pitch trim variables. Figure 10 demonstrates the wake structure under different blade pre-index angles predicted by the LBM, compared with that of a conventional rotor. To further investigate the effect of different distributions of wake on the induced inflow distributions, the wake isosurface diagrams of the Q-criterion are colored with velocity in the y-direction. The wake flow field of the ECR, due to the introduction of the flap, is characterized not only by concentrated tip and root vortex but also by the trailed vortices at flap boundaries. Conversely, the wake flow field of the conventional rotor only demonstrates intense blade root and tip vortex. Moreover, at the blade pre-index angle of 4°, the relatively large flap upward deflection results in a more intense flap tip vortex compared to the situation with the blade pre-index angle of 12°.

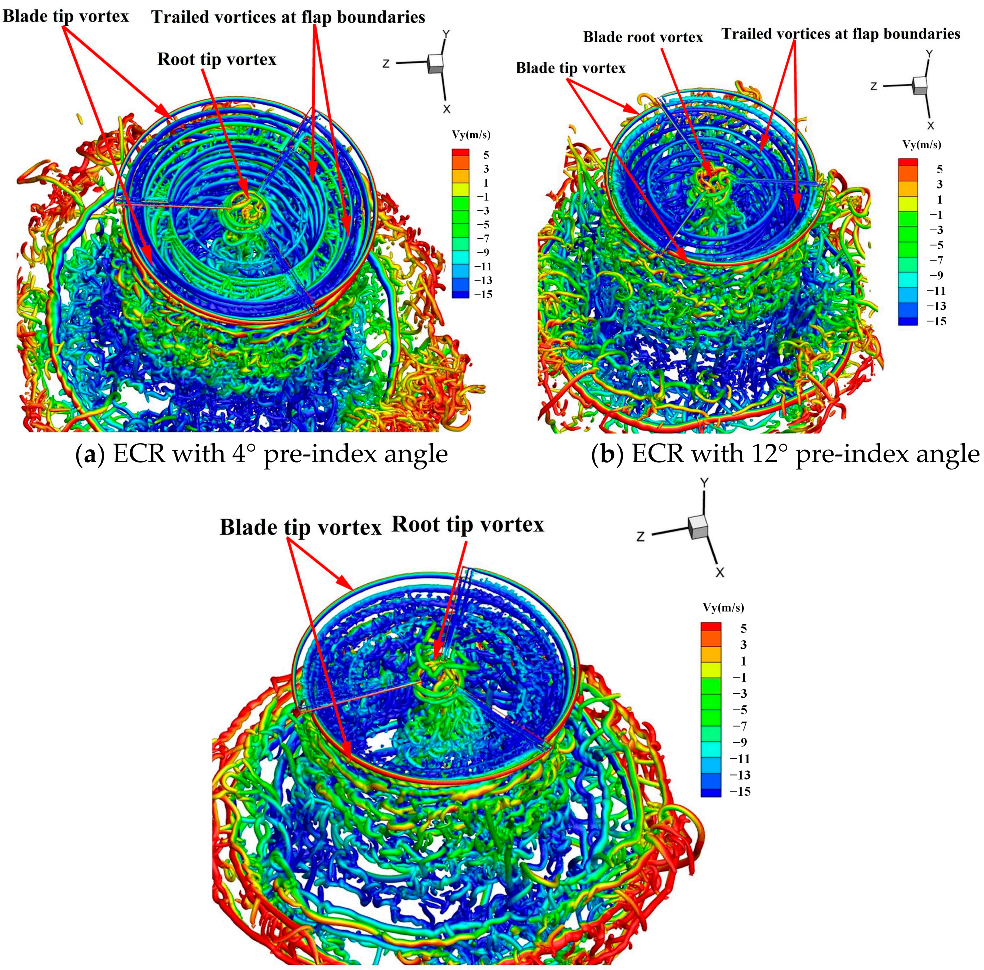

(**a**) ECR with 4° pre-index angle (**b**) ECR with 12° pre-index angle

(**c**) Conventional rotor

Figure 10. Wake flow field of rotors in hovering conditions.

Figure 11 illustrates the time-averaged disc-plane-induced inflow distribution of ECR under different blade pre-index angles, with that of conventional rotor for comparison. At the blade pre-index angle of 4°, due to the influence of intense wake vorticity shed from both ends of the flap, the induced inflow in the flap segment decreases while an increasing trend of the induced inflow can be observed at the exteriors of the flap segment. The maximum value of the induced velocity occurs in the region adjacent to the flap segment. As the blade pre-index angle increases to 12°, the disc-plane-induced inflow distributions contrast with the situation of the blade pre-index angle of 4°; the intense flap tip vortex shed from both sides of the flap results in the increase in induced inflow in the flap segment, while simultaneously decreasing the induced flow in the region adjacent to the flap segment. The maximum induced inflow in the entire disc plane is situated in the flap segment, and the prominent upwash emerges near the blade tip due to the wake contraction. In addition, it can also be observed that the induced inflow distributions of the conventional rotor exhibit a uniform distribution. Therefore, the aforementioned results demonstrate that the distribution of ECR-induced inflow will significantly change due to the flap deflection compared to the conventional rotor, and the intense flap wake vorticity at flap boundaries is the main reason for this phenomenon.

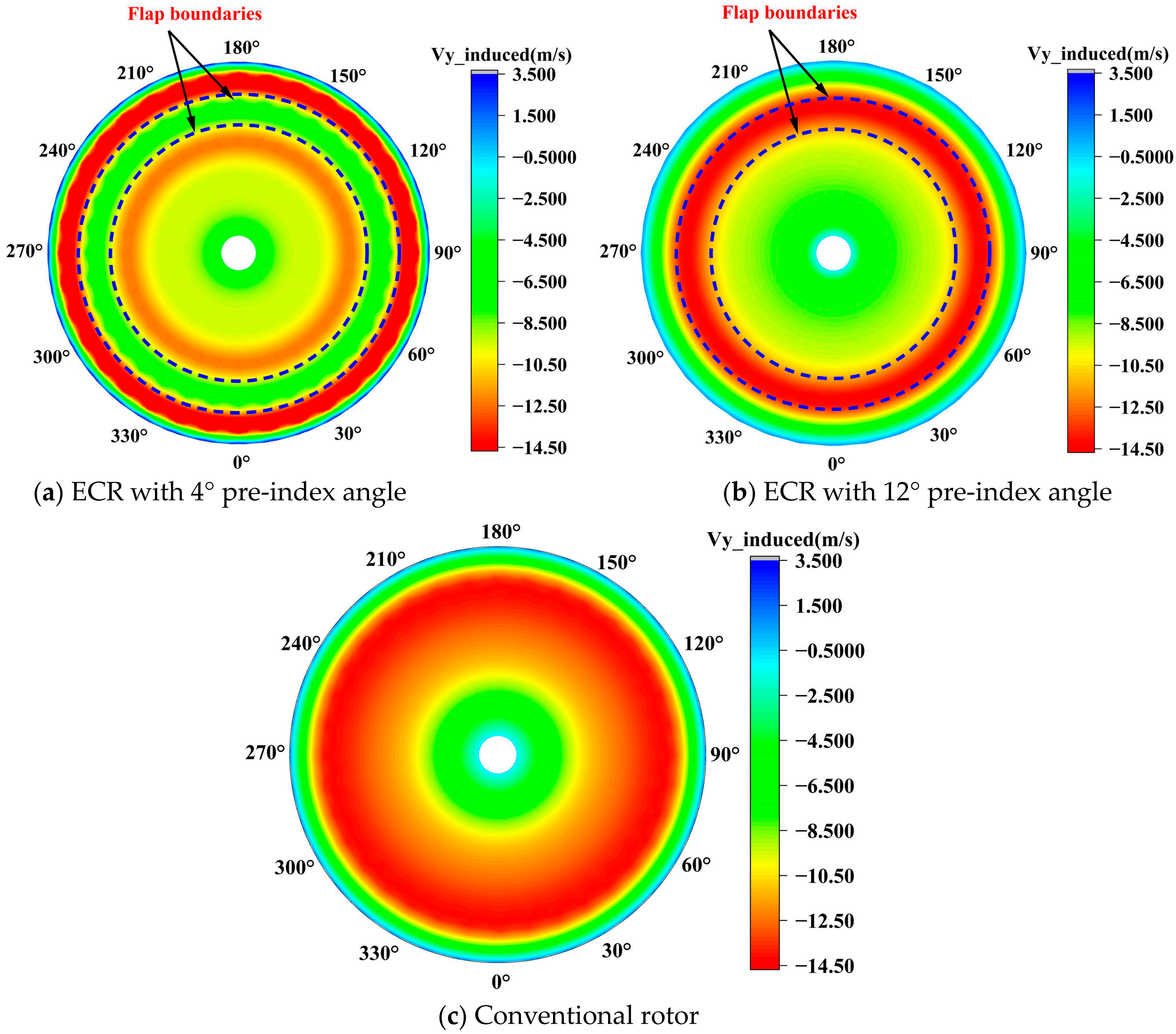

Figure 11. Disc-induced inflow distributions in hovering conditions.

The aerodynamic load distributions on the disc plane under various blade pre-index angles, with the conventional rotor for comparison, are presented in Figure 12. The results show that the aerodynamic load distribution significantly differs due to the flap deflection. At the pre-index angle of 4°, the aerodynamic loads demonstrate a significant decrease in the flap segment, which can be attributed to the large upward deflection of the flap generating considerable additional negative lift. Meanwhile, compared to the conventional rotor, the aerodynamic load at the exteriors of the flap segment increases significantly due to the larger blade pitch. At the blade pre-index angle of 12°, the flap deflects downward to generate additional lift, increasing the load in the flap segment. The aerodynamic load distribution shows no significant difference compared to the conventional rotor, with both exhibiting a uniform distribution. The main reason for this is the relatively small flap deflection and the minor difference in blade pitch between the ECR and conventional rotor.

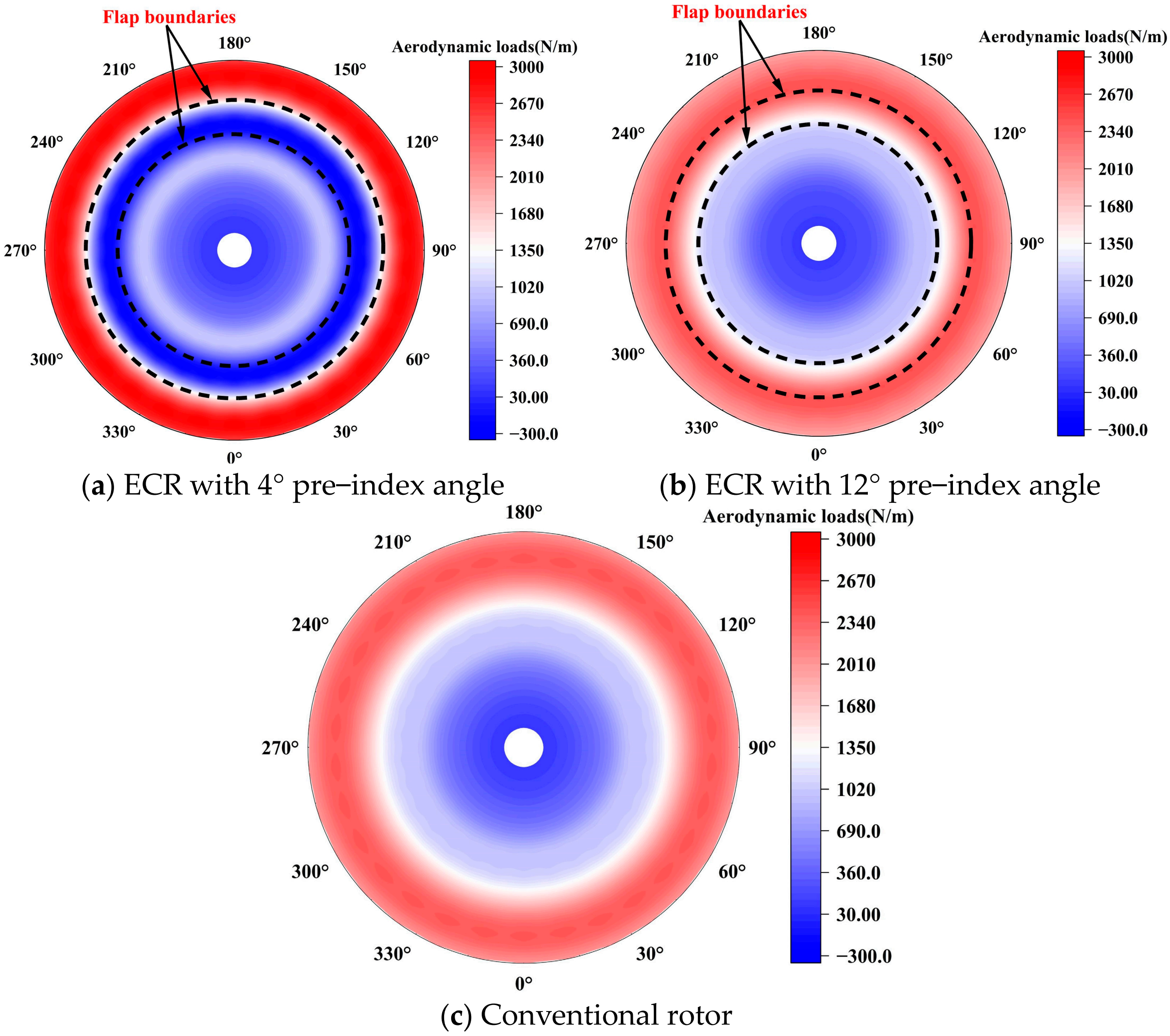

Figure 12. Disc load distributions of rotors in hovering conditions.

3.4. Analysis of ECR Aerodynamic Characteristics in Forward Flight

Building upon the aerodynamic analysis model established in Section 2.2, this section investigates the effects of different advance ratios on the ECR forward flight aerodynamic characteristics. The schemes with advance ratios μ of 0.1 and 0.2 are selected for this study and the blade pre-index angle is set to a constant value of 6°. The trim target variables are the same as the hovering conditions. Therefore, the trim results for the flap collective deflection, lateral cyclic deflection, and longitudinal cyclic deflection under different advance ratios are listed in Table 4.

Table 4. The trim results of the ECR under different advance ratios.

Advance Ratios	Collective Deflection/°	Lateral Cyclic Deflection/°	Longitudinal Cyclic Deflection/°
0.1	−2.39	−4.22	4.17
0.2	−2.43	−2.19	6.16

Figure 13 presents the variations in the flap deflections and ECR blade pitches versus the azimuth angles under different advance ratios. It can be observed that the flap deflections and blade pitches under various advance ratios demonstrate similar characteristics, with a small absolute value at the advancing side and a large absolute value at the retreating side. At the advancing side, the flap initially deflects upward to generate the nose-up moment to increase the blade pitch for trim; as the blade pitch in the trim state decreases, the flap deflection decreases accordingly. When the desired blade pitch trim variable is less than the blade pre-index angle of 6°, corresponding to the positive flap deflection, meaning that the flap deflects downward, generating the nose-down moment to decrease the blade pitch to achieve trim condition. Similarly, the situation of the retreating side can be analyzed. Furthermore, as the forward flight speed increases, the asymmetry of the velocity distributions between the advancing side and the retreating side increases, causing a larger flap downward deflection at the advancing side, generating increased nose-down moment to reduce the blade pitch and a larger upward deflection at the retreating side generating increased nose-up moment to increase the blade pitch.

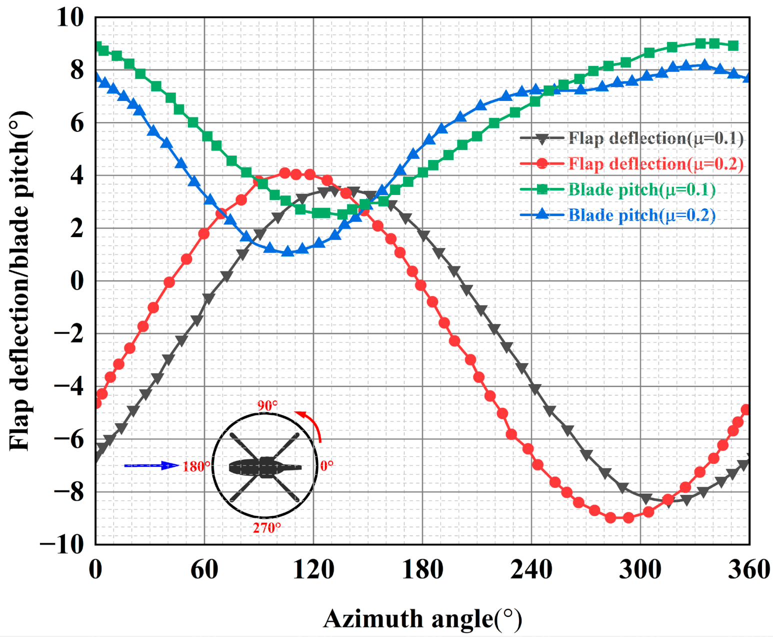

Figure 13. Variation in the ECR blade pitch and flap deflection versus azimuth in forward flight conditions.

The distributions of the ECR wake in the flow field vary under different advance ratios due to the different blade pitches and flap deflections at different azimuth angles. Figure 14 presents the ECR vorticity isosurface diagrams of the wake flow field colored with velocity in the y-direction under various advance ratios. It can be observed that, at the advance ratio of 0.1, the relatively small flap deflection at an azimuth of 90° results in no intense wake vorticity shed from the flap. In contrast, at the azimuth of 0°, the intense flap tip vortices can be observed due to the relatively large flap deflection caused by the superposition of the flap lateral cyclic deflection and flap collective deflection. Moreover, the intense roll-up vortex primarily formed by the blade tip vortex can be observed on both the advancing and retreating sides. As the advance ratio increases to 0.2, at the azimuth of 90°, there are no apparent blade tip vortices due to the relatively small blade pitch, while the intense flap tip vortices shed from both ends of the flap can be observed. Similar to the situation with an advance ratio of 0.1, the visible roll-up vortices are also formed on both the advancing and retreating sides. On the advancing side, the roll-up vortex is primarily formed by the flap wake vortex, whereas on the retreating side, although the flap tip vortices are conspicuous, the roll-up vortex is mainly formed by the wake vortex shed from the blade. The intensity of the roll-up vortex on the retreating side is diminished compared to that when the advance ratio is 0.1.

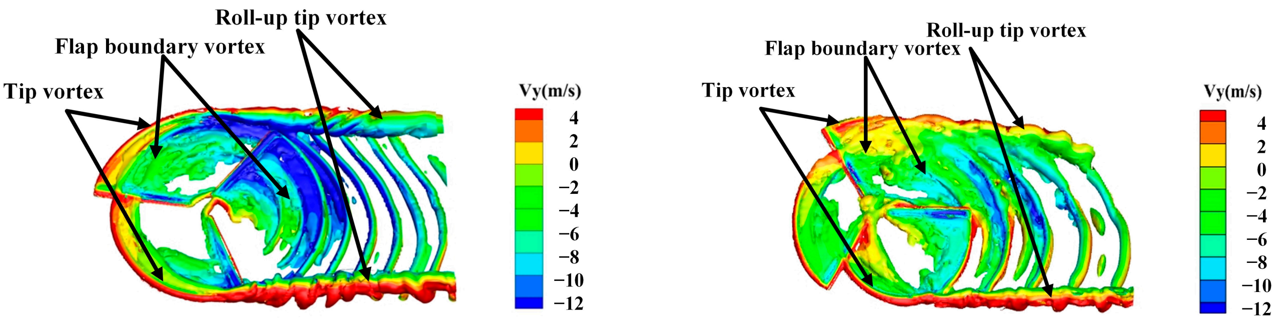

(**a**) μ = 0.1 (**b**) μ = 0.2

Figure 14. Wake flow field of the ECR in forward flight conditions.

Figure 15 shows the time-averaged disc-plane-induced inflow distribution of the ECR under various advance ratios. It can be observed that the distributions of induced inflow within the ECR disc plane follow the characteristics of upwash at the front of the disc plane and downwash at the rear, with the maximum induced inflow occurring at the rear. As the advance ratio increases, the rotor wake, which induces the downwash at the disc rear, is rapidly blown away from the disc plane, causing a decreased trend of the downwash at the disc rear. However, due to the effect of the intense blade tip vortices and flap tip vortices at flap boundaries near the 90° azimuth, the upwash in the exterior region of the flap at the advancing side exhibits an increased trend.

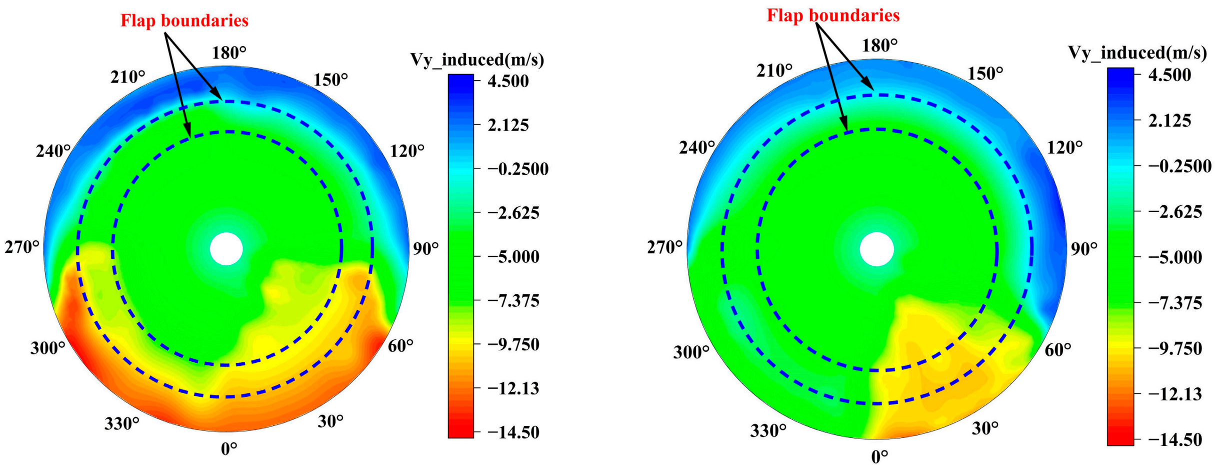

(**a**) μ = 0.1 (**b**) μ = 0.2

Figure 15. Disc-induced inflow distributions of the ECR in forward flight conditions.

Figure 16 presents the disc load distributions under different advance ratios. The result shows that due to the differences in blade pitch and flap deflection at various azimuth angles, the aerodynamic load distribution on the disc plane demonstrates a substantial discrepancy. However, at both advance ratios, the load distributions at the advancing and retreating sides exhibit significant asymmetry, which will intensify as the advance ratio increases. On the advancing side, the blade pitch at the advance ratio of 0.1 is larger compared to the situation of 0.2, causing the increase in the aerodynamic load at the exteriors of the flap segment. Nevertheless, the load at the flap segment at both advance ratios decreases dramatically due to the large upward flap deflection. Moreover, as the advance ratio increases to 0.2, it can also be observed that the aerodynamic load at the exteriors of the flap segment near the azimuth angle of 120° significantly reduces due to the small blade pitch and relatively large blade twist. On the retreating side, the disc load distribution shows no significant difference between both advance ratios, except near the azimuth angle of 210°, where the blade pitch at the advance ratio of 0.2 is larger, resulting in an increase in the aerodynamic load at the exteriors of the flap segment.

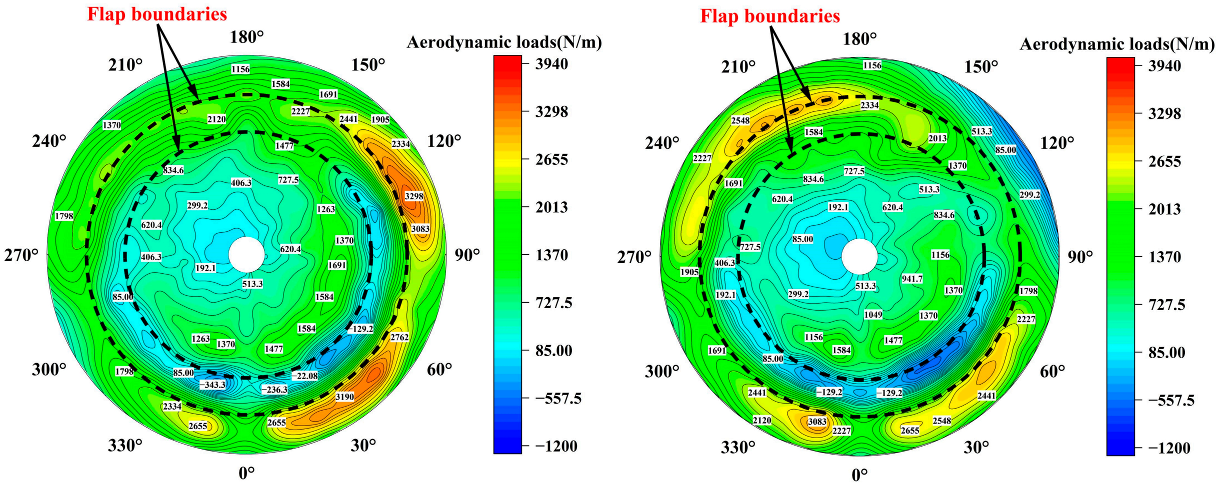

(**a**) μ = 0.1 (**b**) μ = 0.2

Figure 16. Disc load distributions of the ECR under different advance ratios.

4. Conclusions

In this paper, the aerodynamic analysis model of the ECR is developed based on the LBM, and the effects of the flap deflection are taken into account with the refined wall lattice resolution. On this basis, the adaptive wake-refinement strategy is employed to track the evolution of the wake and capture more details of wake structure in the ECR wake flow field. As there are no relevant experimental data regarding the ECR aerodynamic characteristics, to further validate the aerodynamic analysis model based on the LBM, the Caradonna–Tung rotor and 2MRTS rotor tests are selected as references to validate the aerodynamic analysis model established based on the LBM. The results indicate that the LBM can accurately calculate the induced inflow and blade load and adequately predict the rotor wake structure. Therefore, the aerodynamic characteristics of the ECR under hover and forward flight conditions are analyzed based on this model, and the conclusions are provided as follows:

(1) The aforementioned validation results of the convention rotors in hover and forward flight conditions demonstrate the feasibility of the LBM to be employed for simulating the unsteady rotor flow field and analyzing the rotor aerodynamic characteristics. Its results perform with the fine computational accuracy as other aerodynamic analysis methods.

(2) In hovering conditions, the wake flow field of the ECR is characterized not only by concentrated tip and root vortex but also by wake vortex shed from both ends of the flap. The additional flap wake vortex significantly changes the disc-induced inflow distribution. The flap upward deflection causes a decrease in the induced inflow at the flap segment, while the flap downward deflection increases the induced inflow at the flap segment. Additionally, a relatively small flap deflection will not cause significant changes in the disc load distribution when there is a minor difference in blade pitch between the ECR and conventional rotor. However, a relatively large flap upward deflection will significantly reduce the blade aerodynamic load at the flap segment.

(3) At different advance ratios, the distribution of the wake vortex in the ECR flow field varies due to the differences in blade pitch and flap deflection at various azimuths, which further influence the distribution of the induced inflow and aerodynamic load. Moreover, when the advance ratio is small, the roll-up vortex at both sides of the disc is mainly formed by the blade tip vortex. As the advance ratio increases, the flap wake vortex will also form a roll-up vortex.

(4) The adaptive wake-refinement strategy employed in this study can effectively track the evolution of the wake and accurately capture the details of the wake flow field. However, the higher level of the wake refinement may increase the numerical solution time and require a large amount of computational resources. Therefore, the lattice resolution needs to be appropriately arranged during the process of the numerical simulation.

Author Contributions: Methodology, L.W. and T.S.; investigation, writing—original draft preparation, and formal analysis, L.W.; supervision and resources, T.S.; writing—review and editing, T.S.; funding acquisition, T.S. All authors have read and agreed to the published version of the manuscript.

Funding: This research was funded by the Double Thousand Plan Program of Jiangxi Province, (No. jxsq2023101100).

Data Availability Statement: The data that support this study are available from the corresponding author upon reasonable request.

Acknowledgments: This work was supported by the Jiangxi Double Thousand Plan Program (jxsq2023101100). We would like to express our gratitude to Hong Li from Jiangxi Aircraft Airworthiness Certification Center for his guidance and support during the process of the manuscript revision.

Conflicts of Interest: The authors declare no conflict of interest.

References

1. Ormiston, R.A.; Rutkowski, M. Aeroelastic considerations for rotorcraft primary control with on-blade elevons. In Proceedings of the American Helicopter Society 57th Annual Forum Proceedings, Washington, DC, USA, 9–11 May 2001.
2. Shen, J.; Chopra, I. Swashplateless Helicopter Rotor with Trailing-Edge Flaps. *J. Aircr.* **2004**, *41*, 208–214. [CrossRef]
3. Kessler, C. Active rotor control for helicopters: Individual blade control and swashplateless rotor designs. *CEAS Aeronaut. J.* **2011**, *1*, 23–54. [CrossRef]
4. Viswamurthy, S.R.; Ganguli, R. An optimization approach to vibration reduction in helicopter rotors with multiple active trailing edge flaps. *Aerosp. Sci. Technol.* **2004**, *8*, 185–194. [CrossRef]
5. Ma, J.; Lu, Y.; Su, T.; Guan, S. Experimental research of active vibration and noise control of electrically controlled rotor. *Chin. J. Aeronaut.* **2021**, *34*, 106–118. [CrossRef]
6. Patt, D.; Liu, L.; Friedmann, P.P. Simultaneous Vibration and Noise Reduction in Rotorcraft Using Aeroelastic Simulation. *J. Am. Helicopter Soc.* **2006**, *51*, 127–140. [CrossRef]
7. Ravichandran, K.; Chopra, I.; Wake, B.E.; Hein, B. Trailing-Edge Flaps for Rotor Performance Enhancement and Vibration Reduction. *J. Am. Helicopter Soc.* **2013**, *58*, 1–13. [CrossRef]
8. Liu, L.; Friedmann, P.P.; Kim, I.; Bernstein, D.S. Rotor Performance Enhancement and Vibration Reduction in Presence of Dynamic Stall Using Actively Controlled Flaps. *J. Am. Helicopter Soc.* **2008**, *53*, 338–350. [CrossRef]
9. Shen, J.; Yang, M.; Chopra, I. Swashplateless Helicopter Rotor System with Trailing-Edge Flaps for Flight and Vibration Controls. *J. Aircr.* **2006**, *43*, 346–352. [CrossRef]
10. Shen, J.; Chopra, I. A Parametric Design Study for a Swashplateless Helicopter Rotor with Trailing-Edge Flaps. *J. Am. Helicopter Soc.* **2004**, *49*, 43–53. [CrossRef]
11. Shen, J.; Chopra, I. Aeroelastic Modeling of Trailing-Edge-Flap Helicopter Rotors Including Actuator Dynamics. *J. Aircr.* **2004**, *41*, 1465–1472. [CrossRef]
12. Falls, J. *Design and Performance Prediction of Swashplateless Helicopter Rotors with Trailing Edge Flaps and Tabs*; University of Maryland: College Park, MD, USA, 2010.
13. Bagai, A. *Contributions to the Mathematical Modeling of Rotor Flow Fields Using a Pseudo-Implicit Free-Wake Analysis*; University of Maryland: College Park, MD, USA, 1995.
14. Falls, J.; Chopra, I. Piezobimorph actuated servotab for controlling a trailing edge flap. In Proceedings of the 46th AIAA/ASME/ASCE/AHS/ASC Structures, Structural Dynamics and Materials Conference Proceedings, Austin, TX, USA, 18–21 April 2005. [CrossRef]
15. Su, T.; Lu, Y.; Ma, J.; Guan, S. Aerodynamic characteristics analysis of electrically controlled rotor based on viscous vortex particle method. *Aerosp. Sci. Technol.* **2020**, *97*, 105645. [CrossRef]
16. Grunau, D.; Chen, S.; Eggert, K. A lattice Boltzmann model for multiphase fluid flows. *Phys. Fluids A Fluid Dyn.* **1993**, *5*, 2557–2562. [CrossRef]
17. Gunstensen, A.K.; Rothman, D.H.; Zaleski, S.; Zanetti, G. Lattice Boltzmann model of immiscible fluids. *Phys. Rev. A* **1991**, *43*, 4320–4327. [CrossRef]
18. Raabe, D. Overview of the lattice Boltzmann method for nano- and microscale fluid dynamics in materials science and engineering. *Model. Simul. Mater. Sci. Eng.* **2004**, *12*, R13–R46. [CrossRef]

19. Romani, G.; Casalino, D. Rotorcraft blade-vortex interaction noise prediction using the Lattice-Boltzmann method. *Aerosp. Sci. Technol.* **2019**, *88*, 147–157. [CrossRef]
20. van der Velden, W.; Romani, G.; Casalino, D. Validation and insight of a full-scale S-76 helicopter rotor using the Lattice-Boltzmann Method. *Aerosp. Sci. Technol.* **2021**, *118*, 107007. [CrossRef]
21. Thibault, S.; Holman, D.; Garcia, S.; Trapani, G. CFD simulation of a quad-rotor UAV with rotors in motion explicitly modeled using an LBM approach with adaptive refinement. In Proceedings of the 55th AIAA Aerospace Sciences Meeting Proceedings, Grapevine, TX, USA, 9–13 January 2017. [CrossRef]
22. Bhatnagar, P.L.; Gross, E.P.; Krook, M. A Model for Collision Processes in Gases. I. Small Amplitude Processes in Charged and Neutral One-Component Systems. *Phys. Rev. B* **1954**, *94*, 511–525. [CrossRef]
23. Geier, M.; Greiner, A.; Korvink, J.G. A factorized central moment lattice Boltzmann method. *Eur. Phys. J. Spec. Top.* **2009**, *171*, 55–61. [CrossRef]
24. Premnath, K.N.; Banerjee, S. Incorporating forcing terms in cascaded lattice Boltzmann approach by method of central moments. *Phys. Rev. E* **2009**, *80*, 036702. [CrossRef]
25. Chen, S.; Doolen, G.D. Lattice boltzmann method for fluid flows. *Annu. Rev. Fluid Mech.* **1998**, *30*, 329–364. [CrossRef]
26. Qian, Y.H.; D'Humières, D.; Lallemand, P. Lattice BGK Models for Navier-Stokes Equation. *Europhys. Lett.* **1992**, *17*, 479–484. [CrossRef]
27. Suga, K.; Kuwata, Y.; Takashima, K.; Chikasue, R. A D3Q27 multiple-relaxation-time lattice Boltzmann method for turbulent flows. *Comput. Math. Appl.* **2015**, *69*, 518–529. [CrossRef]
28. Bao, Y.B.; Meskas, J. *Lattice Boltzmann Method for Fluid Simulations*; Department of Mathematics, Courant Institute of Mathematical Sciences, New York University: New York, NY, USA, 2011; Volume 44.
29. Ducros, F.; Nicoud, F.; Poinsot, T. Wall-adapting local eddy-viscosity models for simulations in complex geometries. *Numer. Methods Fluid Dyn.* **1998**, *6*, 293–299.
30. Caradonna, F.X.; Tung, C. Experimental and analytical studies of a model helicopter rotor in hover. In Proceedings of the European Rotorcraft and Powered Lift Aircraft Forum, Bristol, UK, 16–19 September 1980; No. A-8332.
31. Whitehouse, G.R. Investigation of Hybrid Grid–Based Computational Fluid Dynamics Methods for Rotorcraft Flow Analysis. *J. Am. Helicopter Soc.* **2011**, *56*, 1–10. [CrossRef]
32. Elliott, J.W.; Althoff, S.L.; Sailey, R.H. *Inflow Measurements Made with a Laser Velocimeter on a Helicopter Model in Forward Flight*; volume 1: Rectangular planform blades at an advance ration of 0.15; No. NASA-TM-100541; NASA: Washington, DC, USA, 1988.
33. Lee, B.S.; Choi, J.H.; Kwon, O.J. Numerical Simulation of Free-Flight Rockets Air-Launched from a Helicopter. *J. Aircr.* **2011**, *48*, 1766–1775. [CrossRef]
34. Kenyon, A.R.; Brown, R.E. Wake Dynamics and Rotor-Fuselage Aerodynamic Interactions. *J. Am. Helicopter Soc.* **2009**, *54*, 12003. [CrossRef]